KORC Modeling of Wall Heating by Avalanche Runaway Electrons During a Final Loss Event in DIII-D

Matt Beidler[1]

With much input from D. del-Castillo-Negrete[1], D. Shiraki[1], E. Hollmann[2], and L. Baylor[1]

[1]Oak Ridge National Laboratory
[2]University of California San Diego

This manuscript has been authored by UT-Battelle, LLC, under contract DE-AC05-00OR22725 with the US Department of Energy (DOE). The US government retains and the publisher, by accepting the article for publication, acknowledges that the US government retains a nonexclusive, paid-up, irrevocable, worldwide license to publish or reproduce the published form of this manuscript, or allow others to do so, for US government purposes. DOE will provide public access to these results of federally sponsored research in accordance with the DOE Public Access Plan (http://energy.gov/downloads/doe-public-access-plan).

This work was supported by the US DOE using the DIII-D National Fusion Facility, a DOE Office of Science user facility, under contract DE-FC02-04ER54698 and used resources of the National Energy Research Scientific Computing Center (NERSC), a US Department of Energy Office of Science User Facility operated under Contract No. DE-AC02-05CH11231.

Secondary REs are the dominant contribution to large PFC surface heating in rapid loss event of DIII-D

- **Rapid RE final loss event in DIII-D induces large electric fields in open flux regions that increases generation of secondary REs**
  - Secondary REs rapidly deconfine when generated in open flux region by initial REs with large drift orbit effects

- **Secondary REs have lower kinetic energy and deposit their energy shallowly into PFCs**

- **KORC modeling indicates that secondary REs are dominant contribution to transiently large PFC <u>surface</u> heating**

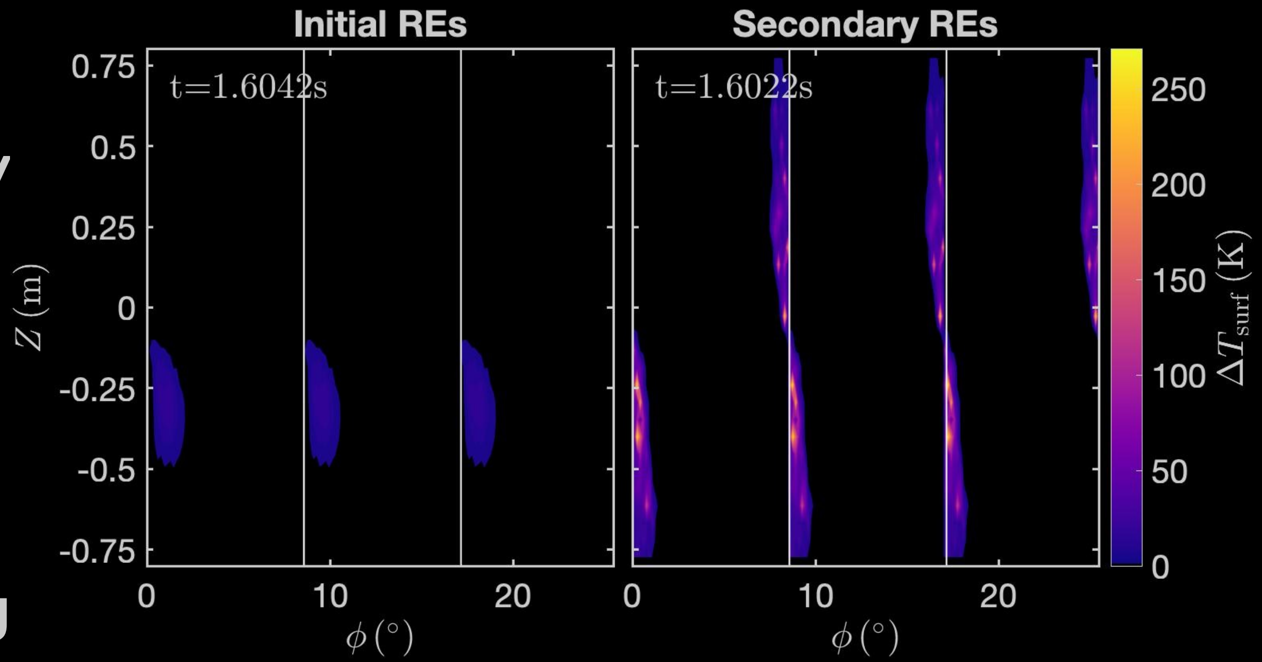

Average surface heating (in toroidal extent) from KORC

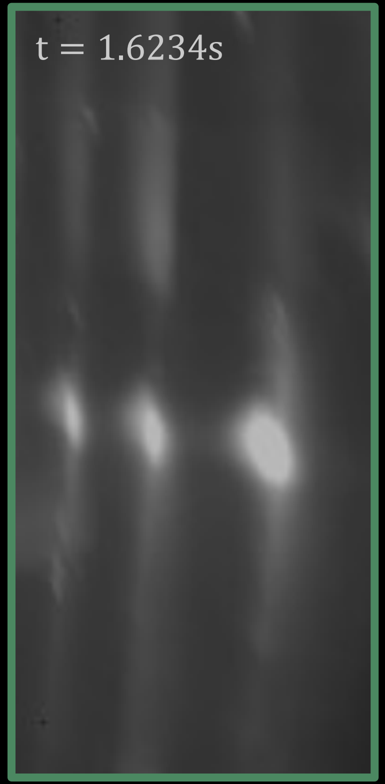

DIII-D infrared imaging

Looking at DIII-D shot 177031 with D2 injection into post-disruption RE beam [1]

- Disruption triggered by primary injection of cryogenic Ar pellet
- No impurity purge and recovery of electron density after secondary D2 injection
- Central solenoid stops driving RE beam to trigger rapid final loss event

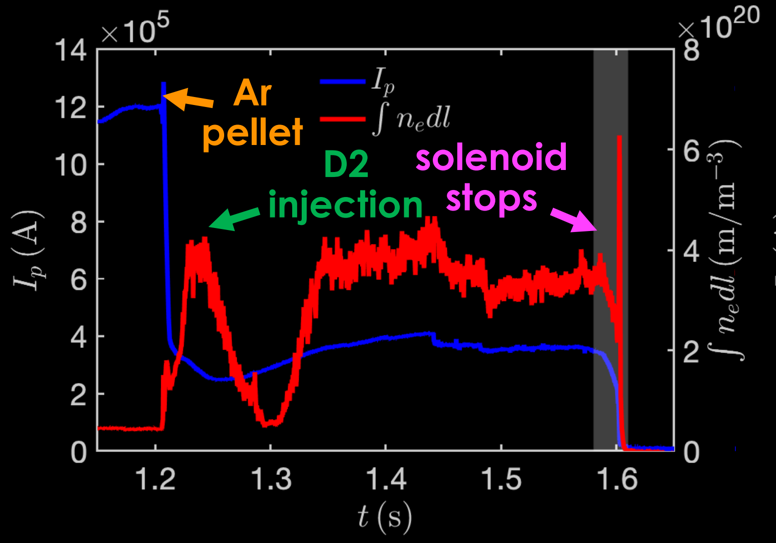

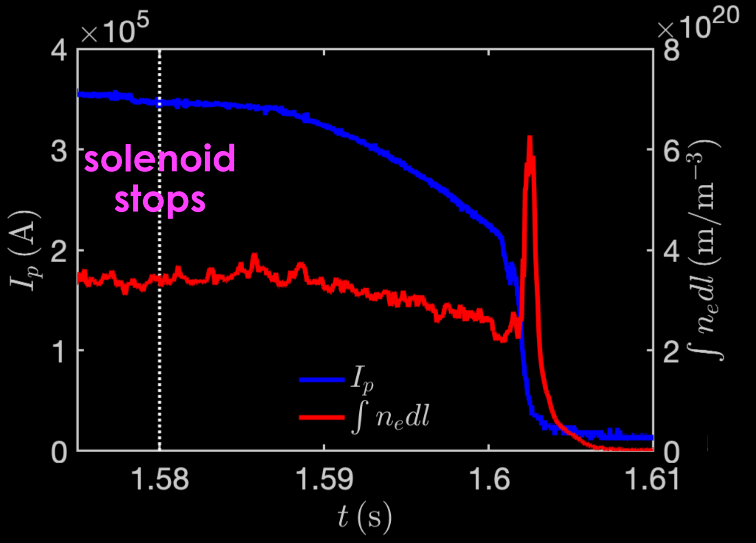

ψ_p contours with E_ϕ colormap

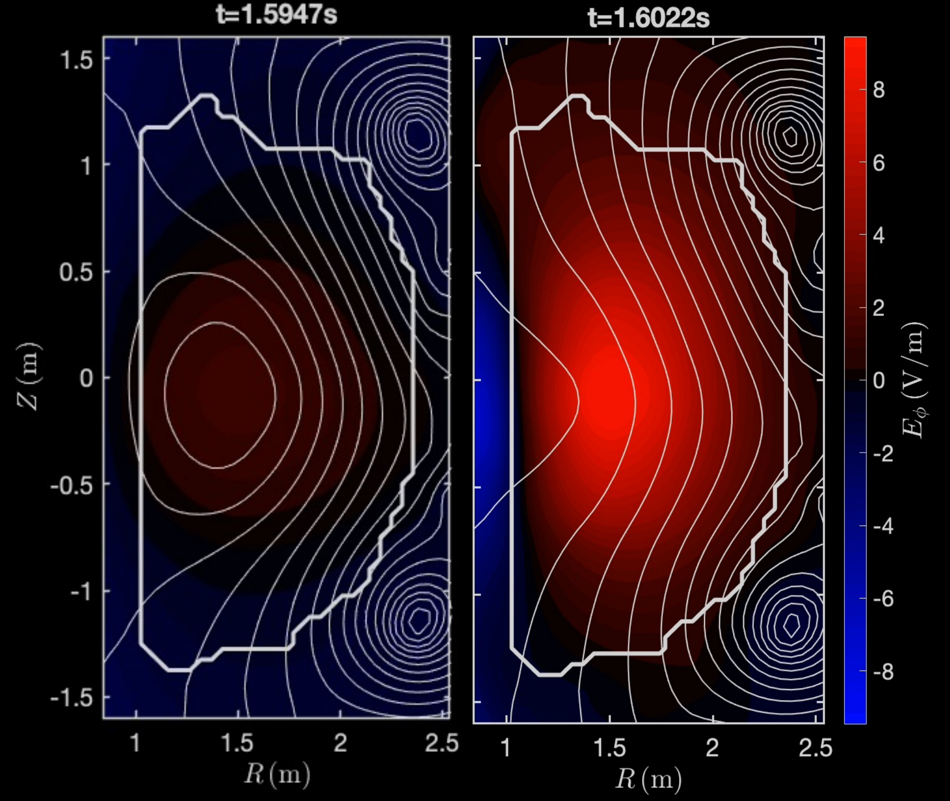

[1]Unmitigated termination in Paz-Soldan et al., *Nucl. Fusion* (2021)

Infrared (IR) imaging shows final loss event localized at leading edge of graphite PFCs

$t = 1.61348$

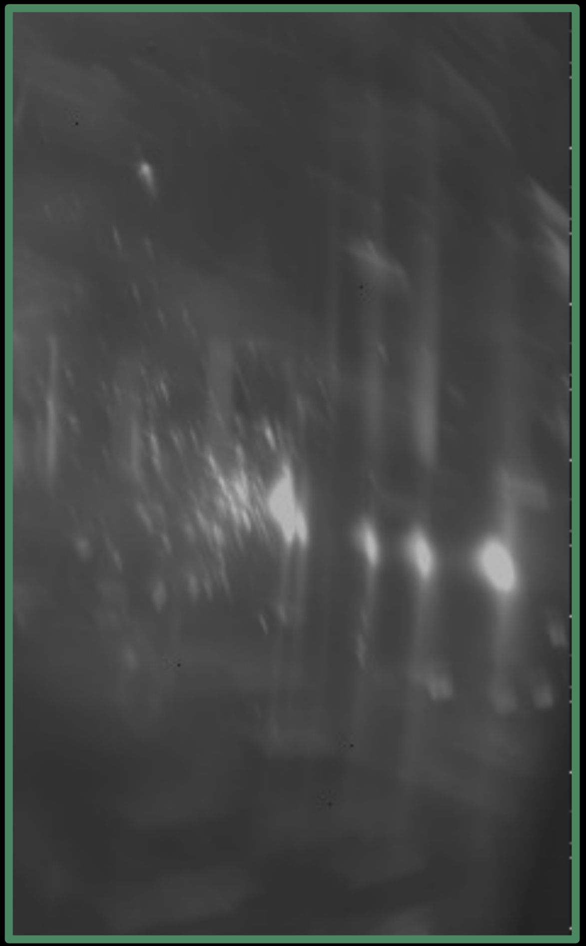

- **IR imaging [1] shows localized RE heating at graphite tile interface**
  - A single tile at one toroidal location appears to ablate while others withstand heating
- **Calculation of T at PFC from IR affected by plasma, obscuring value**
  - IR detector as configured saturates during final loss event
  - DIII-D graphite tiles ablate around 2500 C° [2]

IR PFC T evolution

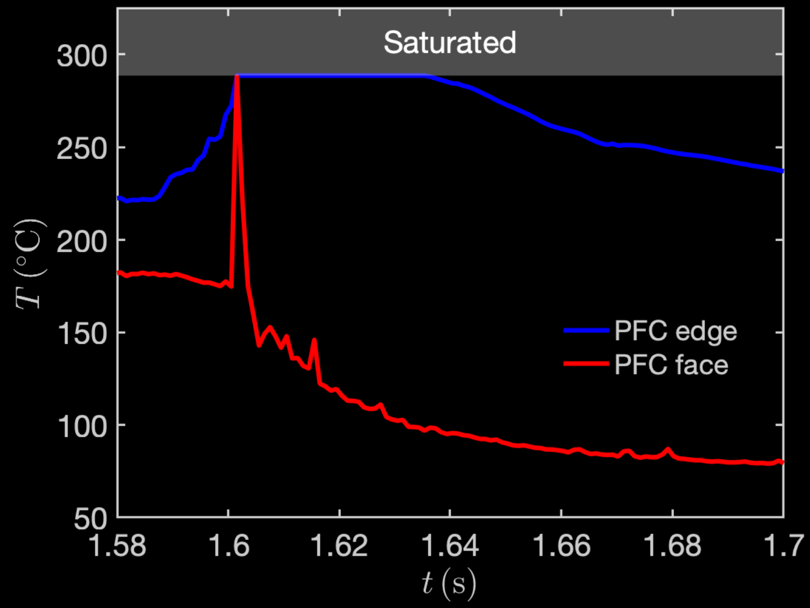

[1] Courtesy of C. Lasnier (LLNL) [2] Luxon, *Nucl. Fusion* (2002)

Rapid RE final loss event increases inductive electric fields and secondary electron generation via avalanche source

- **Approximate RE threshold electric field with impurities**

  $$\mathbf{E_{crit} \cong E_{CH}^{tot} = \frac{n_e^{tot}}{n_e}\frac{m_e c}{e\tau_c} = 3.14V/m\ [1]}$$

  – $\tau_c = \frac{4\pi\varepsilon_0^2 m_e^2 c^3}{n_e e^4 \ln\Lambda}, n_e^{tot} = \sum_s (Z_{s,0} - Z_s) n_s,$
  $n_e = 2.25\times10^{20}\text{m}^{-3}, n_{\text{D}^{+1}} = n_{\text{Ar}^{+1}} = n_{\text{Ar}^{+0}} = n_e/2$

  – Relativistic $\ln\Lambda$ evaluated at $p_{\text{crit}} = m_e c \sqrt[4]{\bar{\nu}_S \bar{\nu}_D} / \sqrt{E/E_{\text{CH}}^{\text{tot}}}$ [2]

- **Approximate RE growth rate due to avalanche REs**

  $$\mathbf{\Gamma_{RP} \cong \left(\frac{n_e^{tot}}{n_e}\right)^2 \frac{1}{\tau_c \ln\Lambda}\left(\frac{E}{E_{CH}^{tot}} - 1\right)(4 + \bar{\nu}_S\bar{\nu}_D)^{-1/2}\ [2]}$$

  – RE population exponentiates in ~7.7ms

- **Secondary REs rapidly deconfined when generated in open flux region from initial REs with large drift orbit effects**

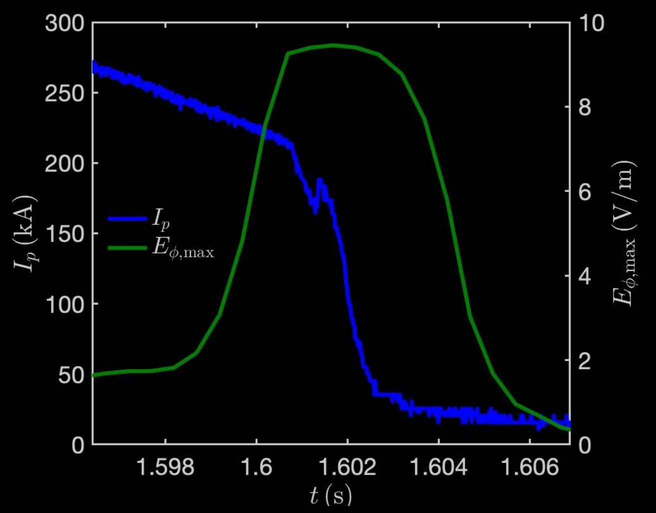

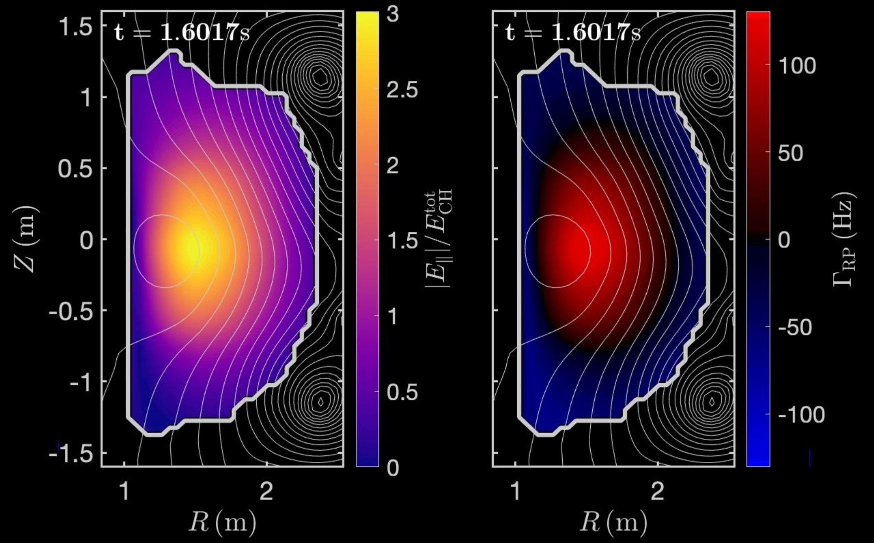

Oak Ridge National Laboratory

[1] Hesslow et al., *Plasma Phys. Control. Fusion* (2018) [2] Hesslow et al., *Nucl. Fusion* (2019)

Avalanche RE distribution results in large surface heating

- **Avalanche distribution is large at low energy, proportional to $\frac{1}{p\gamma(\gamma-1)^2}$ [1]**
  - Secondaries generated below threshold can contribute to heating
  - Approximate threshold from Ref. [2] with critical p_{crit} from Ref. [3]
- **Low energy REs deposit their energy shallowly into PFC**
  - Continuously slowing down approximation (CSDA) from ESTAR database
- **1D analytical surface temperature change of PFCs [4]**
  - $\Delta T_{\text{surf}}(t) = \sum_i \frac{\kappa}{K\delta_i} \int_0^t q_i(t') \exp\left(\frac{\kappa(t-t')}{\delta_i^2}\right) \text{erfc}\left(\frac{\sqrt{\kappa(t-t')}}{\delta_i}\right) dt'$
  - Assumes exponentially-decreasing volumetric energy deposition

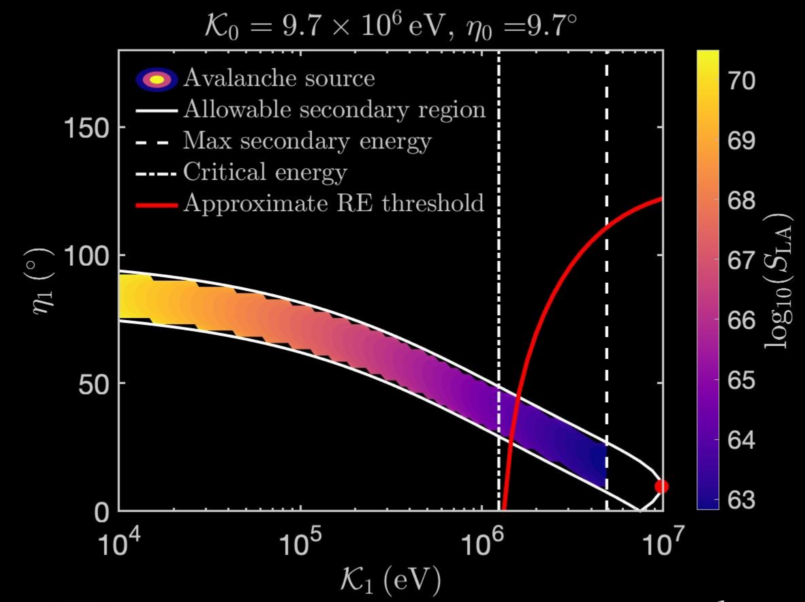

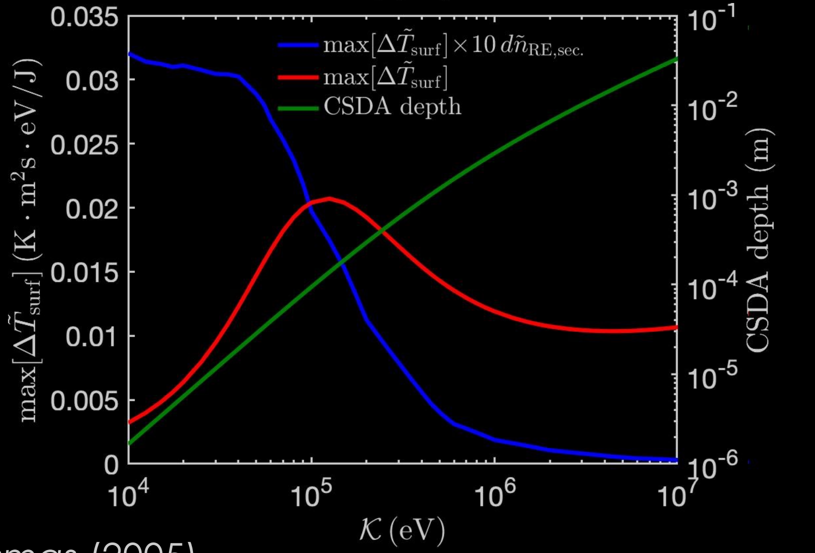

OAK RIDGE National Laboratory

[1] Aleynikov et al., *IAEA FEC* (2014) [2] Smith et al., *Phys. Plasmas* (2005)
[3] Hesslow et al., *Nucl. Fusion* (2019) [4] Martín-Solís et al., *Nucl. Fusion* (2014)

KORC modeling of RE final loss event uses evolving fields and constant/uniform density profiles

- **KORC evolves RE guiding center (GC) orbits using time-sequenced JFIT reconstructions [1]**
  - RE beam with uniform, mono-energy/pitch $10\mathrm{MeV}/10°$ initial distribution
  - Axisymmetric fields don't capture small MHD activity [2] during final loss event
- **Partially-ionized impurities included in collision operators**
  - Assume constant and uniform plasma and Ar profiles, including neutrals
    - $n_e = 2.25\times10^{20}\mathrm{m}^{-3}$ from DIII-D interferometer, $T_e = 1.5\mathrm{eV},\ n_{\mathrm{Ar}^{+1}} = n_{\mathrm{Ar}^{+0}} = n_{\mathrm{D}^{+1}} = 1.125\times10^{20}\mathrm{m}^{-3}$
  - Increases collisionality and electrons available for secondary generation
- **Set minimum momentum for numerical tractability of resolving collision processes**
  - "Thermalize" particles dropping below scaled-down global $p_{\mathrm{crit,global}}$
  - Sample avalanche distribution with minimum dependent on scaled-down local $p_{\mathrm{crit,local}}$ to find convergent results
- **Analytic model of faceted inner wall developed in KORC as regular polygon**
  - $15\mathrm{cm}$ width graphite tiles yield difference between radius of leading edge and tile center of $< 3\mathrm{mm}$

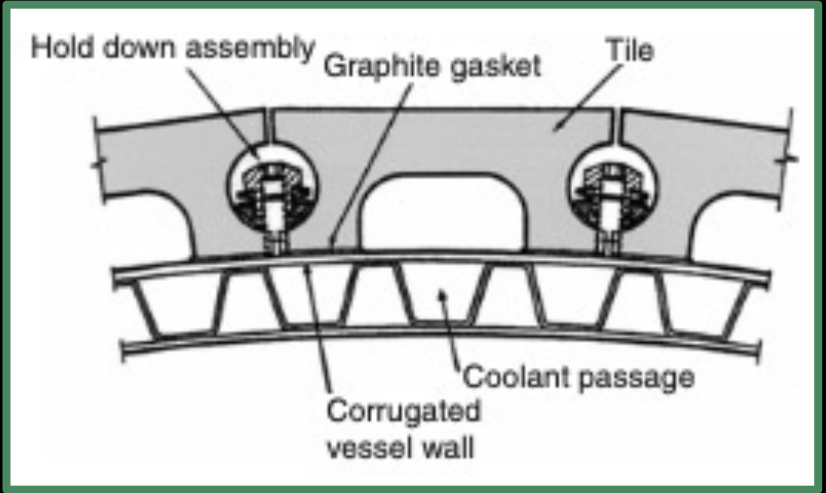

Schematic of faceted graphite tiles [3]

OAK RIDGE National Laboratory

[1] Beidler et al., *Phys. Plasmas* (2020) [2] Paz-Soldan et al., *Nucl. Fusion* (2021) [3] Luxon, *Nucl. Fusion* (2002)

Secondary REs generated in open flux regions during final loss event are rapidly deconfined

- **Flux surfaces closed at beginning of final loss event**
  - Most secondary REs thermalize rapidly

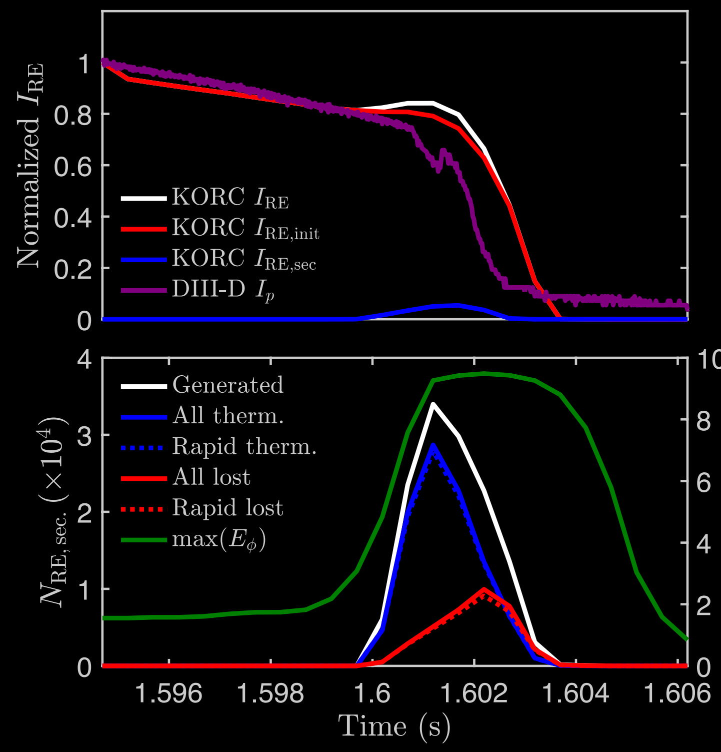

- **Initial REs travel through open flux regions due to drift orbit effects at high energies**
  - Secondary REs at lower energy with no drift orbit effects are rapidly deconfined
  - Number of deconfined secondaries converges below $0.035 p_{crit,global}$ (not shown)

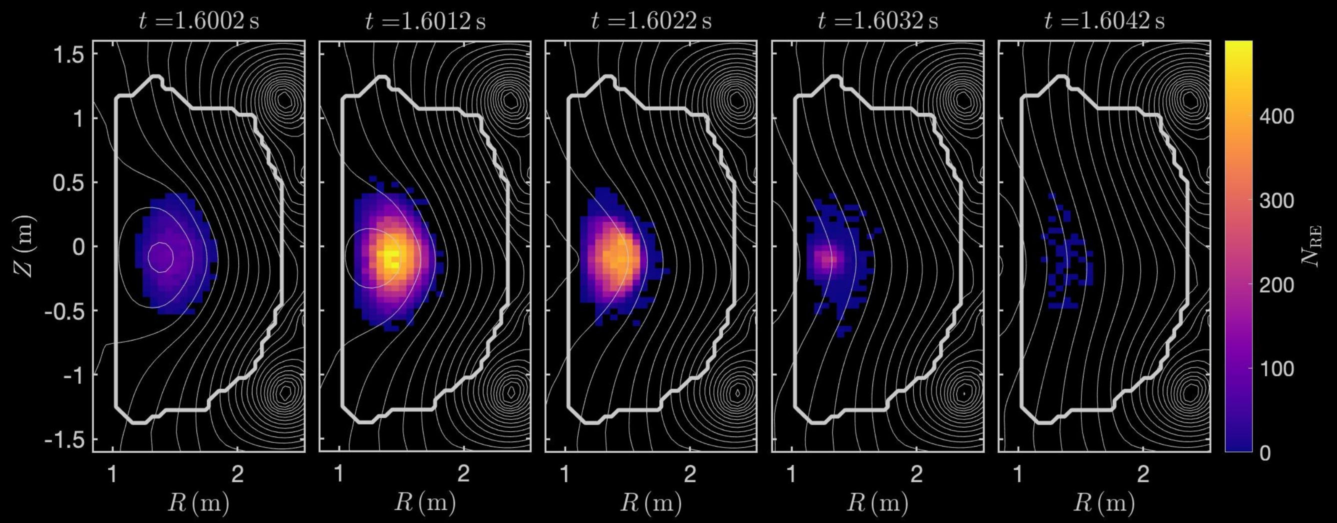

Secondary REs generated each 0.5ms

OAK RIDGE National Laboratory

Estimate angle of incidence to PFC from guiding center angle of incidence

- ΔT_{surf} is sum of contributions from each deconfined RE
  - $\Delta T_{\mathrm{surf}}(\vec{X},t) = \sum_i \frac{\kappa}{K\delta_i} \int_0^t q_i(\vec{X},t') \exp\left(\frac{\kappa(t-t')}{\delta_i^2}\right) \mathrm{erfc}\left(\frac{\sqrt{\kappa(t-t')}}{\delta_i}\right) dt'$
  - q_i is power flux of REs scaled to match initial simulation and experimental current
  - $\delta_i = \delta_{\mathrm{ESTAR}}(\mathrm{KE}_i) \sin \Theta_i$
- **Angle of incidence Θ from GC angle of incidence θ_{GC}, pitch η, and randomly-chosen gyrophase χ**
  - $\sin \Theta_i = -\cos \theta_{\mathrm{GC},i} \sin \eta_i \sin \chi_i + \sin \theta_{\mathrm{GC},i} \cos \eta_i$
  - Linear interpolation of trajectory with wall yields θ_{GC}
  - Also require that $\sin \Theta_i > 0$, putting constraint on possible χ_i
  - Split every RE into 10 with different randomly-chosen gyrophases

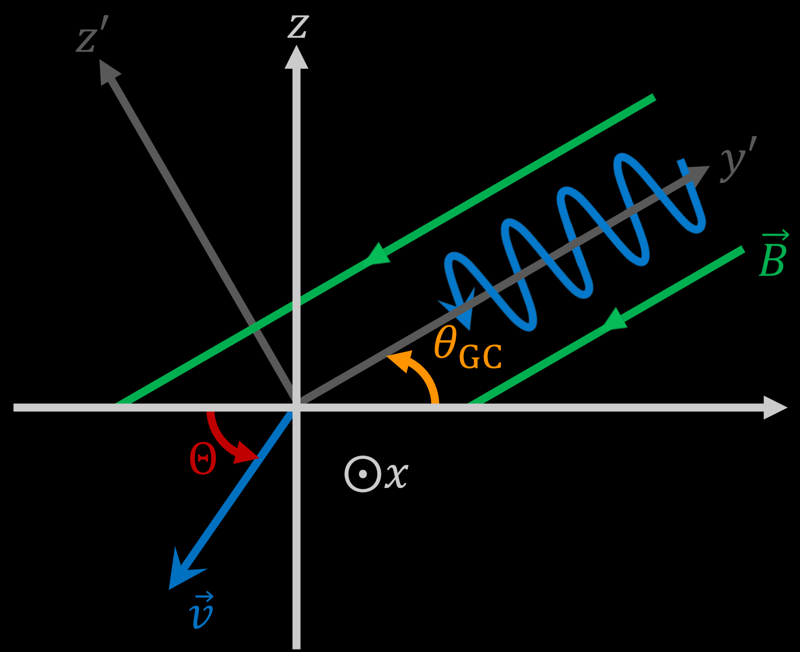

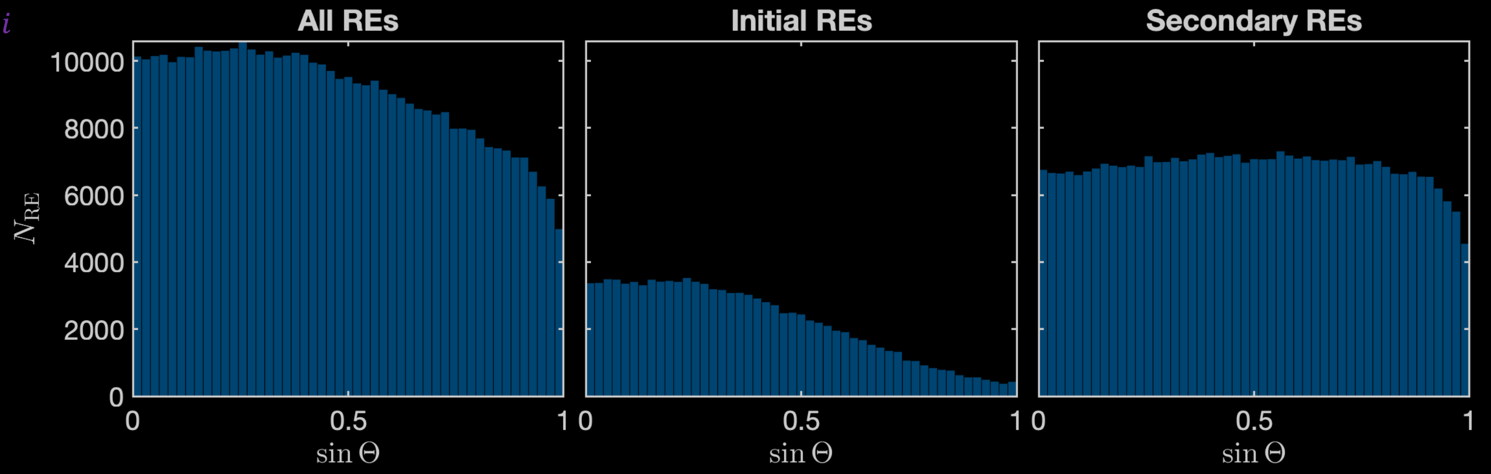

Secondary RE heating is on leading edge and required for qualitative agreement with experimental observations

- **Uniform toroidal spacing of tiles enables projecting all orbits onto a single tile**
  - Still many tiles in vertical direction
- **PFC surface heating due to secondary REs is order of magnitude and half larger than that due to initial REs**
- **Initial REs have $\eta_i < 90°$, secondary REs can have $\eta_i > 90°$**

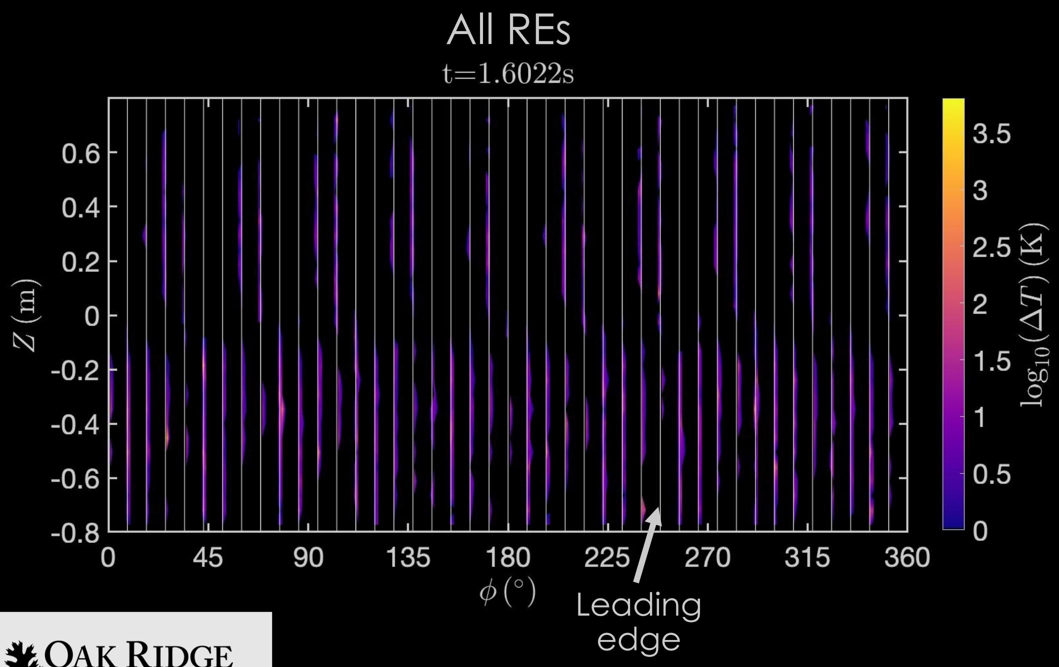

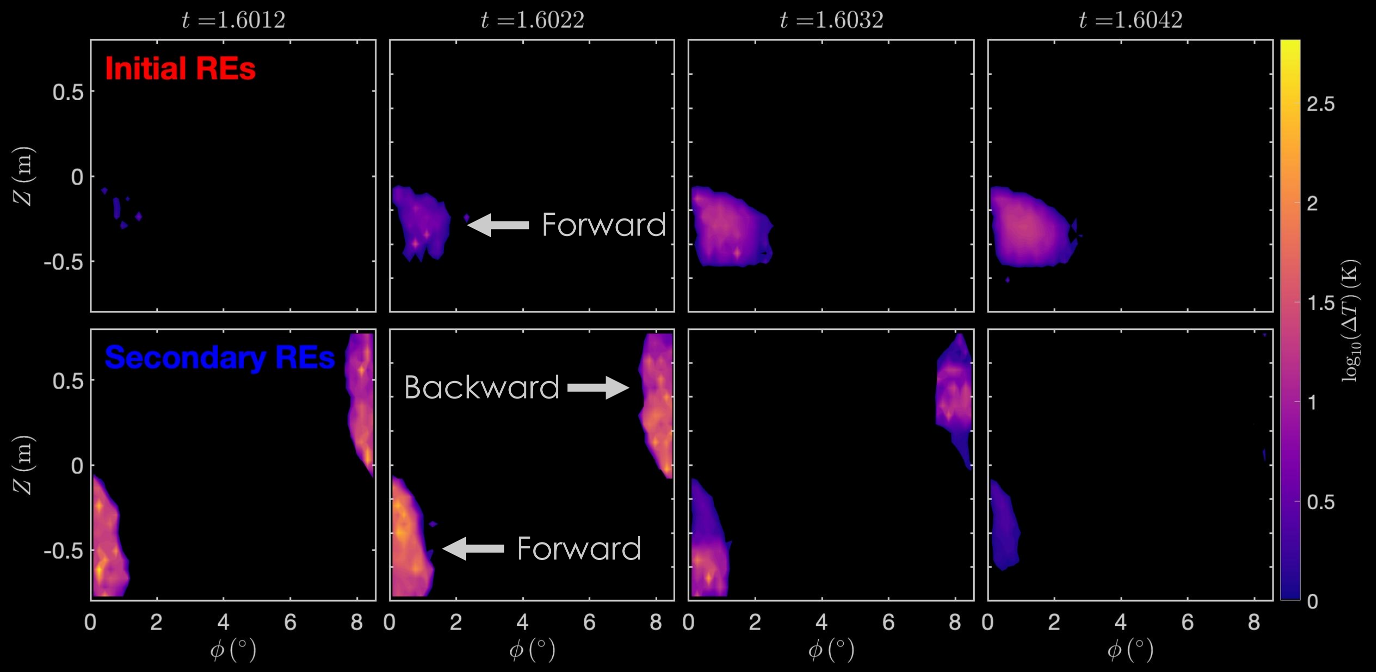

Secondary RE heating is on leading edge and required for qualitative agreement with experimental observations

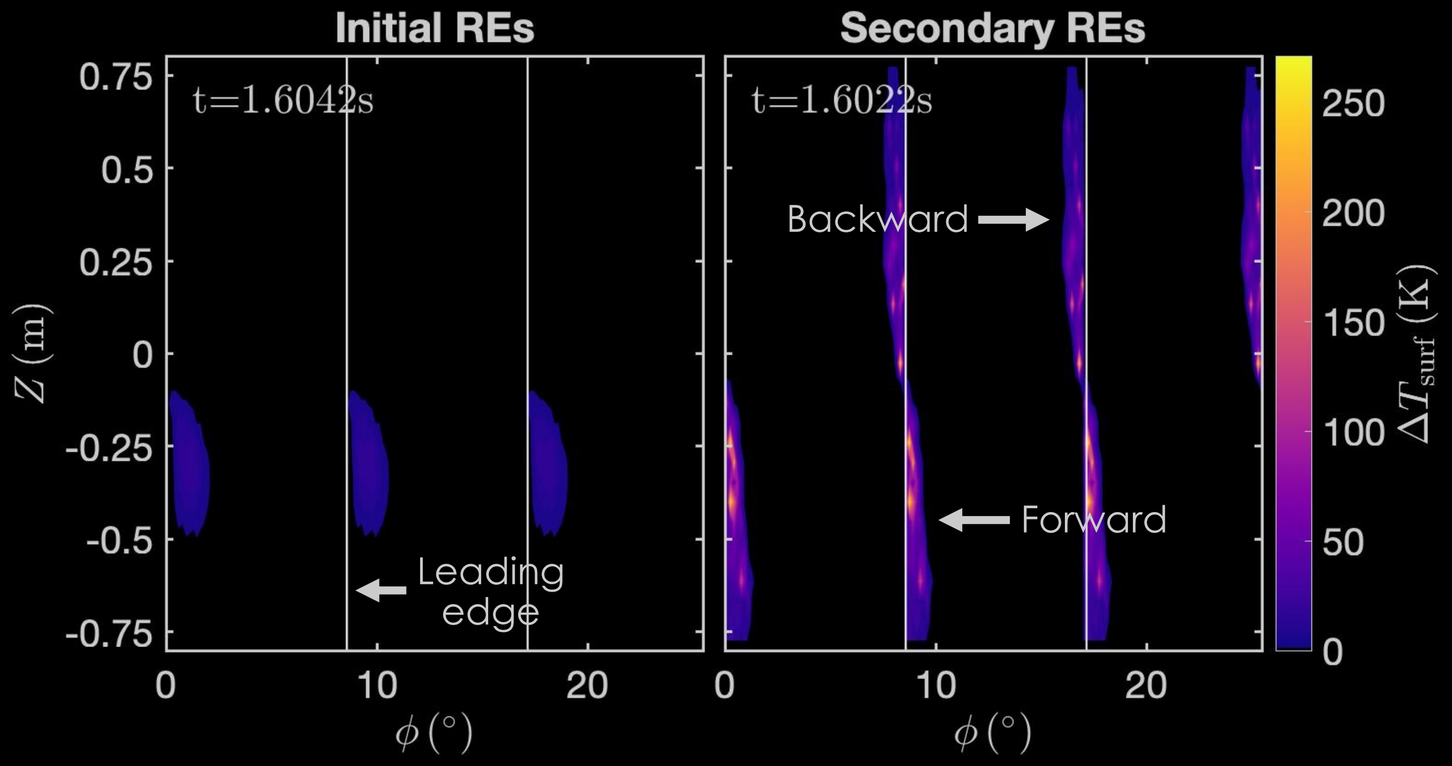

Average surface heating (in toroidal extent) from KORC

DIII-D infrared imaging

Discussion

- **Large electric fields induced on trailing side of advecting RE beam**
  - Induced electric field in region of open flux surfaces
- **Large-angle collisions will generate low-energy secondaries that lead to large wall heating, even if they don't runaway**

Future Work

- **Wall heating of final loss events with 3D MHD (ITPA collaboration MDC-DSOL-1)**
- **Explore how thermalized secondary REs contribute to wall heating**
- **Explore how wall irregularities change local heating**
- **Couple with 1D diffusion model to include experimentally-inferred plasma and impurity profiles**
- **Use KORC results in more advanced volumetric energy deposition and heat transfer/fluid motion codes**
- **Explore sensitivity to charging of wall by deconfined REs and partially-ionized impurities**
- **Self-consistent kinetic-MHD modeling to simulate RE beam scrape off and deconfinement due to 3D MHD modes**

Secondary REs are the dominant contribution to large PFC surface heating in rapid loss event of DIII-D

- **Rapid RE final loss event in DIII-D induces large electric fields in open flux regions that increases generation of secondary REs**
  - Secondary REs rapidly deconfine when generated in open flux region by initial REs with large drift orbit effects
- **Secondary REs have lower kinetic energy and deposit their energy shallowly into PFCs**
- **KORC modeling indicates that secondary REs are dominant contribution to transiently large PFC surface heating**

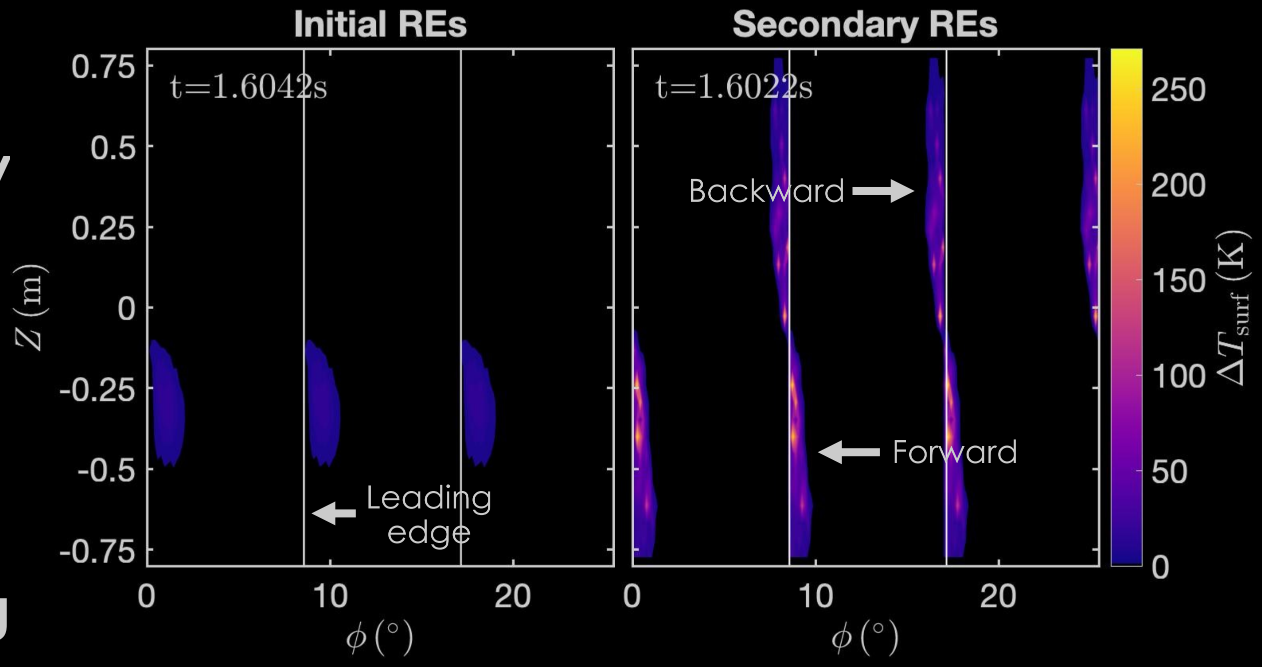

Average surface heating (in toroidal extent) from KORC

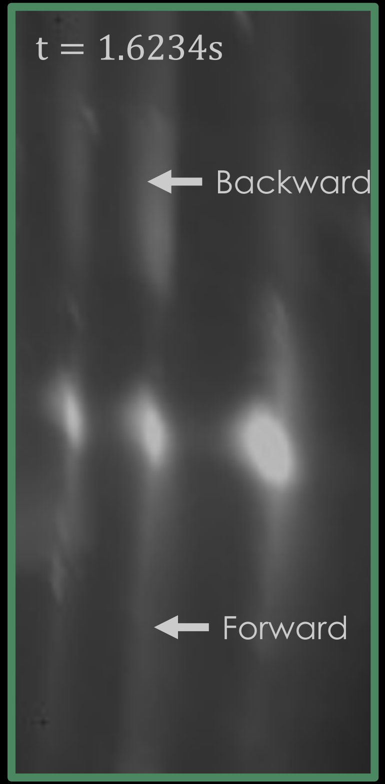

DIII-D infrared imaging

Extra Slides

Orbit effects are necessary for accurate modeling of REs

- **Poloidal plane RE (passing) orbit approximately**

$$(R-\Delta)^2 + Z^2 = R_c^2$$
$$\Delta = R_0 \pm q_0 v_\phi/\Omega_e$$
$$R_c^2 = \Delta^2 - R_0^2 \pm 2q_0 v_\phi/\Omega_e$$

  - $\Omega_e = eB/\gamma m_e\,, \gamma = 1/\sqrt{1-(v/c)^2}$
  - Assumes axisymmetric, circular cross-section with constant q_0, sign depends on B_ϕ direction
  - Canonical toroidal angular momentum conserved without acceleration mechanisms

- **Capture effects of trapped and passing particles**
  - $40\ \mathrm{MeV}$ REs shown with varying pitch angle θ

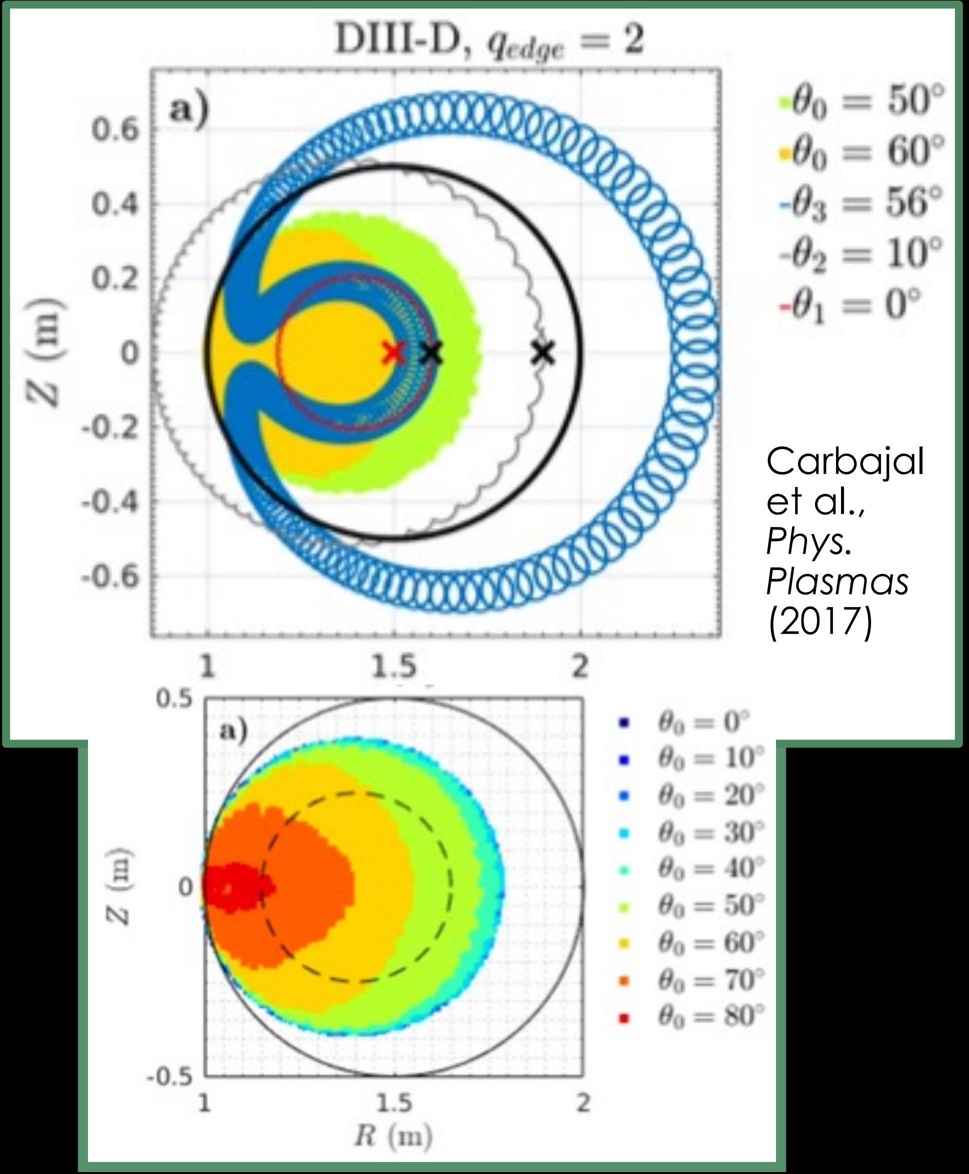

Carbajal et al., *Phys. Plasmas* (2017)

KORC evolves RE orbits with synchrotron radiation to accurately calculate RE transport

- **Relativistic Lorentz force for FO orbits**

$$\frac{d\boldsymbol{X}}{dt} = \boldsymbol{v},\ \frac{d\boldsymbol{p}}{dt} = -e(\boldsymbol{E} + \boldsymbol{v}\times\boldsymbol{B})$$

- **Relativistic GC system of equations**

$$\frac{d\boldsymbol{X}}{dt} = \frac{1}{\boldsymbol{b}\cdot\boldsymbol{B}^*}\left(e\boldsymbol{E}\times\boldsymbol{B} + \frac{m\mu\boldsymbol{b}\times\nabla B + p_\parallel \boldsymbol{B}^*}{m\gamma_{gc}}\right),\ \frac{dp_\parallel}{dt} = \frac{\boldsymbol{B}^*}{\boldsymbol{b}\cdot\boldsymbol{B}^*}\left(e\boldsymbol{E} - \frac{\mu\nabla B}{\gamma_{gc}}\right)$$

  - $\boldsymbol{B}^* = q\boldsymbol{B} + p_\parallel \nabla\times\boldsymbol{b}$, $p_\parallel = \gamma m V \cos\eta$ with pitch angle η, $\mu = p_\perp^2/2mB$, $\gamma_{gc} = \sqrt{1 + (p_\parallel/mc)^2 + 2\mu B/mc^2}$
  - Tao et al., *Phys. Plasmas* (2007)

- **RE synchrotron radiation**

$$\boldsymbol{F}_R = \frac{1}{\gamma\tau_R}\left[(\boldsymbol{p}\times\boldsymbol{b})\times\boldsymbol{b} - \frac{1}{(m_e c)^2}(\boldsymbol{p}\times\boldsymbol{b})^2\boldsymbol{p}\right]$$

  - $\tau_R = 6\pi\epsilon_0(m_e c)^3/(e^4 B^2)$
  - Landau-Lifshitz form of Lorentz-Abraham-Dirac radiation reaction force

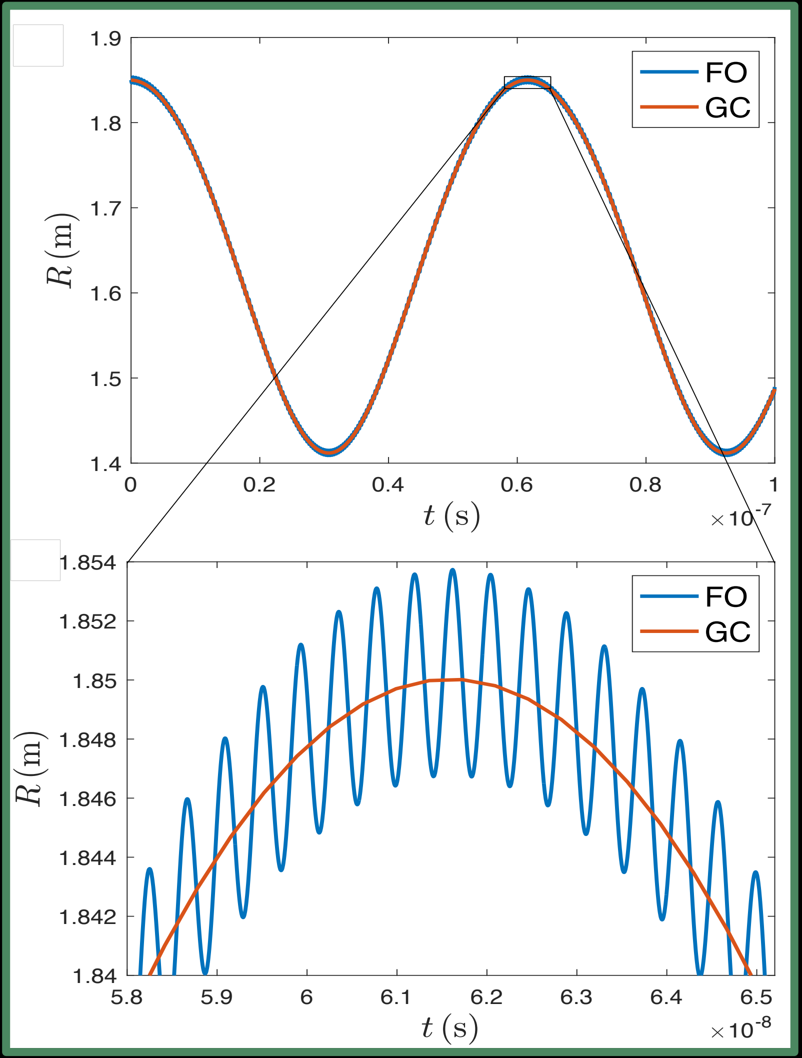

Oak Ridge National Laboratory

KORC includes Coulomb collisions with bound electrons

- **Particle-based (Langevin) linearized Fokker-Planck Coulomb collision operator**

$$dp = \left\{-C_F(p) + \frac{1}{p^2}\frac{\partial}{\partial p}[p^2 C_A(p)]\right\}dt + \sqrt{2C_A(p)}dW_p,$$

$$d\eta = \frac{C_B(p)}{p^2}\cot\eta\, dt + \frac{\sqrt{2C_B(p)}}{p}dW_\eta,$$

  - General transport coefficients [Papp et al., *Nucl. Fusion* (2011)] and bound electron physics [Hesslow et al., *Phys. Rev. Lett.* (2017)]

$$C_F(v) = \frac{\Gamma_{ee}\mathcal{G}\left(\frac{v}{v_{\rm th}}\right)}{T_e}\left\{1 + \sum_j \frac{n_j}{n_e}\frac{Z_j - Z_{0j}}{\ln\Lambda_{ee}}\left[\frac{1}{5}\ln\left(1+h_j^5\right) - \beta^2\right]\right\},\ C_A(v) = \frac{\Gamma_{ee}\mathcal{G}\left(\frac{v}{v_{\rm th}}\right)}{v},$$

$$C_B(v) = \frac{\Gamma_{ei}}{2v}\left(Z_{\rm eff} + \sum_j \frac{n_j}{n_e}\frac{g_j}{\ln\Lambda_{ei}}\right) + \frac{\Gamma_{ee}}{2v}\left[{\rm erf}\left(\frac{v}{v_{\rm th}}\right) - \mathcal{G}\left(\frac{v}{v_{\rm th}}\right) + \frac{1}{2}\left(\frac{v_{\rm th}v}{c^2}\right)^2\right],$$

    - $\Gamma_{ee,ei} = n_e e^4 \ln\Lambda_{\rm ee,ei}/4\pi\epsilon_0^2$ $\mathcal{G}$ is the Chandrasekhar function, n_j is the density of the j-th ionization state, Z_j and Z_{0j} are the fully and partially ionized impurity ion charge, g_j is screening function, h_j is a function describing energy absorption

- **RE bremsstrahlung radiation**

$$\frac{\rm d}{dt}[(\gamma-1)m_e c^2] = -2n_j\kappa Z_{0j}\left(Z_{0j}+1\right)\frac{\alpha}{2}(\gamma-1)\left[\ln(2\gamma) - \frac{1}{3}\right]$$

  - $\kappa = 2\pi r_e^2 m_e c^2$, $r_e = e^2/4\pi\epsilon_0 m_e c^2$, and $\alpha = 1/137$
  - Bakhtiari et al., *Phys. Rev. Lett.* (2005)

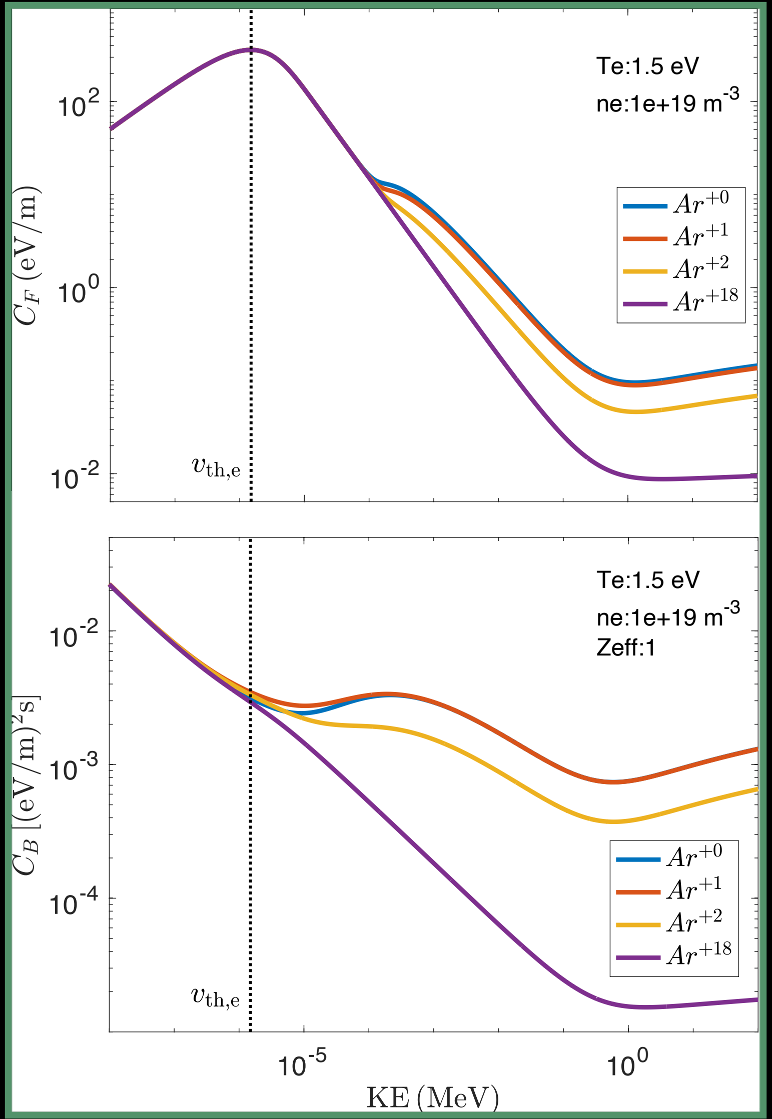

Oak Ridge National Laboratory

Aleynikov et al., IAEA FEC (2014) and Boozer, PoP (2015) developed a more accurate large-angle collision operator

- $\mathcal{S}[f_0(\gamma_0,\xi_0),f_1(\gamma_1,\xi_1)] = \frac{n_e}{2\pi m_e^3 c^2}\frac{1}{p_1\gamma_1}\iiint dp_0 d\xi_0 d\varphi_0 \frac{p_0^3}{\gamma_0}\frac{d\sigma}{d\gamma_1}\delta(\hat{n}_1\cdot\hat{n}_0-\xi_\gamma)f_0(p_0,\xi_0)$
  - Subscript 0 for initial and 1 for secondary RE
  - $\frac{d\sigma}{d\gamma_1} = \frac{2\pi r_e^2}{\gamma_0^2-1}\left[\frac{(\gamma_0-1)^2\gamma_0^2}{(\gamma_1-1)^2(\gamma_0-\gamma_1)^2}-\frac{2\gamma_0^2+2\gamma_0-1}{(\gamma_1-1)(\gamma_0-\gamma_1)}+1\right],\ \xi_\gamma=\sqrt{\frac{\gamma_1-1}{\gamma_1+1}}\sqrt{\frac{\gamma_0+1}{\gamma_0-1}}$
  - $\int d\varphi_0\delta(\hat{n}_1\cdot\hat{n}_0-\xi_\gamma) = \frac{1}{\pi\sqrt{(1-\xi_1^2)(1-\xi_0^2)-(\xi_\gamma-\xi_0\xi_1)^2}}$ is form from Aleynikov et al., IAEA FEC (2014)
- **McDevitt et al., PPCF (2019) adapts this for Monte Carlo by choosing single particle distribution function for each initial RE with index i**
  - $f_0(p_0,\xi_0) = \delta^3(\vec{x}_0-\vec{x}_i)\frac{\delta(p_0-p_i)\delta(\xi_0-\xi_i)}{2\pi p_0^2}$
    - Secondary REs born at location of initial REs
  - $\mathcal{S}[f_i(\gamma_i,\xi_i),f_1(\gamma_1,\xi_1)] = \frac{n_e r_e^2}{2\pi^2 m_e^3 c^2}\frac{1}{p_1\gamma_1}\frac{p_i}{\gamma_i(\gamma_i^2-1)}\left[\frac{(\gamma_i-1)^2\gamma_i^2}{(\gamma_1-1)^2(\gamma_i-\gamma_1)^2}-\frac{2\gamma_i^2+2\gamma_i-1}{(\gamma_1-1)(\gamma_i-\gamma_1)}+1\right]\frac{1}{\sqrt{(1-\xi_1^2)(1-\xi_i^2)-(\xi_\gamma-\xi_i\xi_1)^2}}$

Benchmark implementation of large angle collision operator

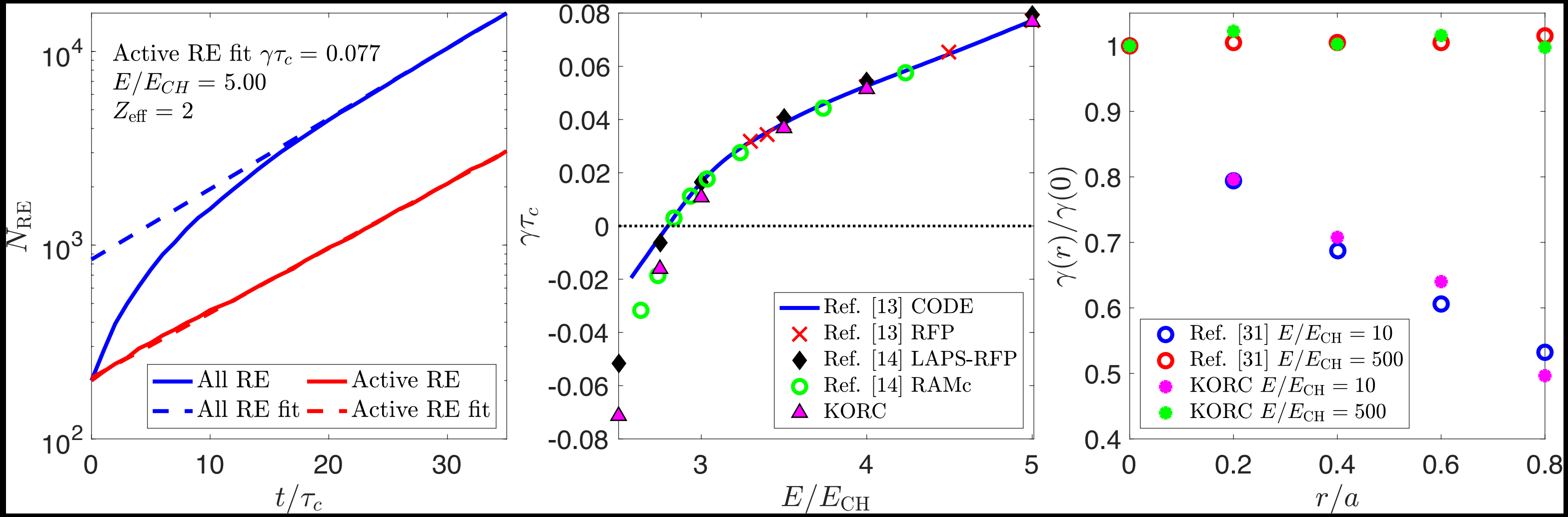

- **Spatially-independent calculations, using electric field acceleration, collisional friction, pitch angle scattering, synchrotron radiation, and large angle collision source**
  - Left plot shows evolution of all (blue trace) and a subpopulation of active (red trace) REs included in a calculation
  - Growth rates in center plot compare favorably with Liu et al., PPCF (2017) and McDevitt et al., PPCF (2019)
- **Toroidal and trapped particle effects on the avalanche growth rate are consistent with simulations in McDevitt and Tang, EPL (2019)**
  - Physical effects discussed in Nilsson et al., JPP (2015) and Nilsson et al., Nucl. Fusion (2015).

Oak Ridge National Laboratory

Approximate impurity content determined in simulations without large angle collision operator

- **Begin KORC calculations near time when solenoid stops driving RE beam**
- **n_e is set from interferometer measurements**
  - Ratio of Ar^{+1} and D^{+1} is unconstrained by experimental diagnostics
- **Set neutral Ar^{+0} to same value as Ar^{+1}**
  - Result from Beidler et al., IAEA FEC (2021)

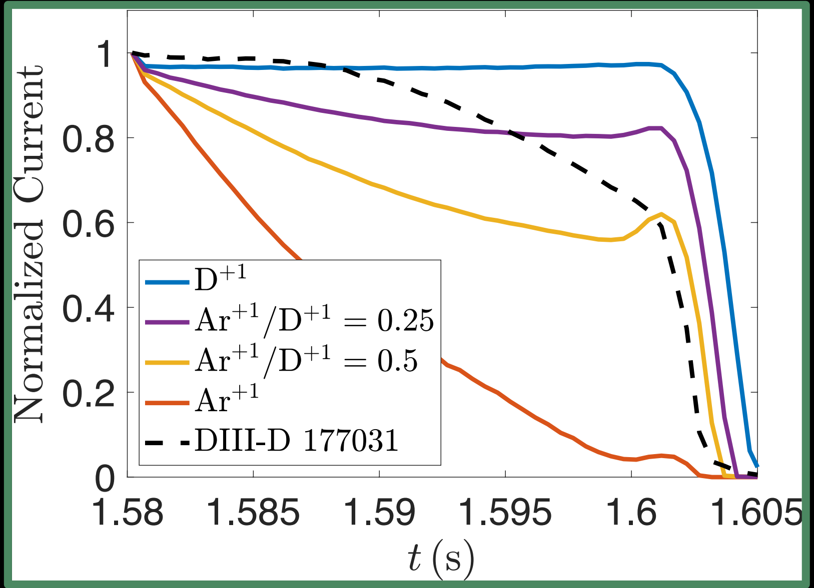

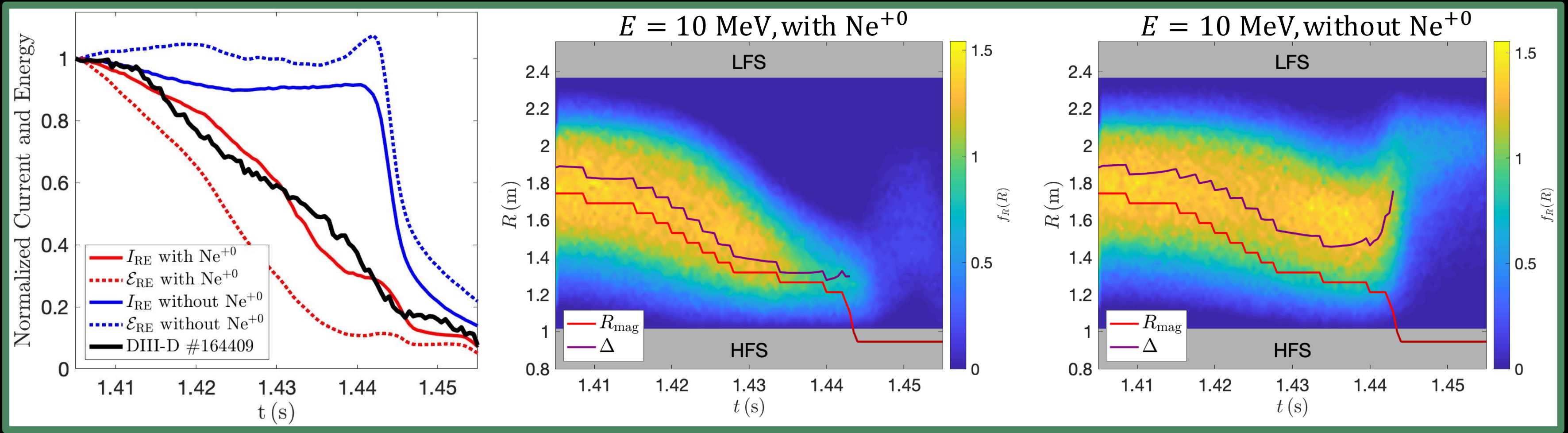

OAK RIDGE National Laboratory

Energy and pitch distribution of secondary REs reaches a quasi-steady state during final loss event

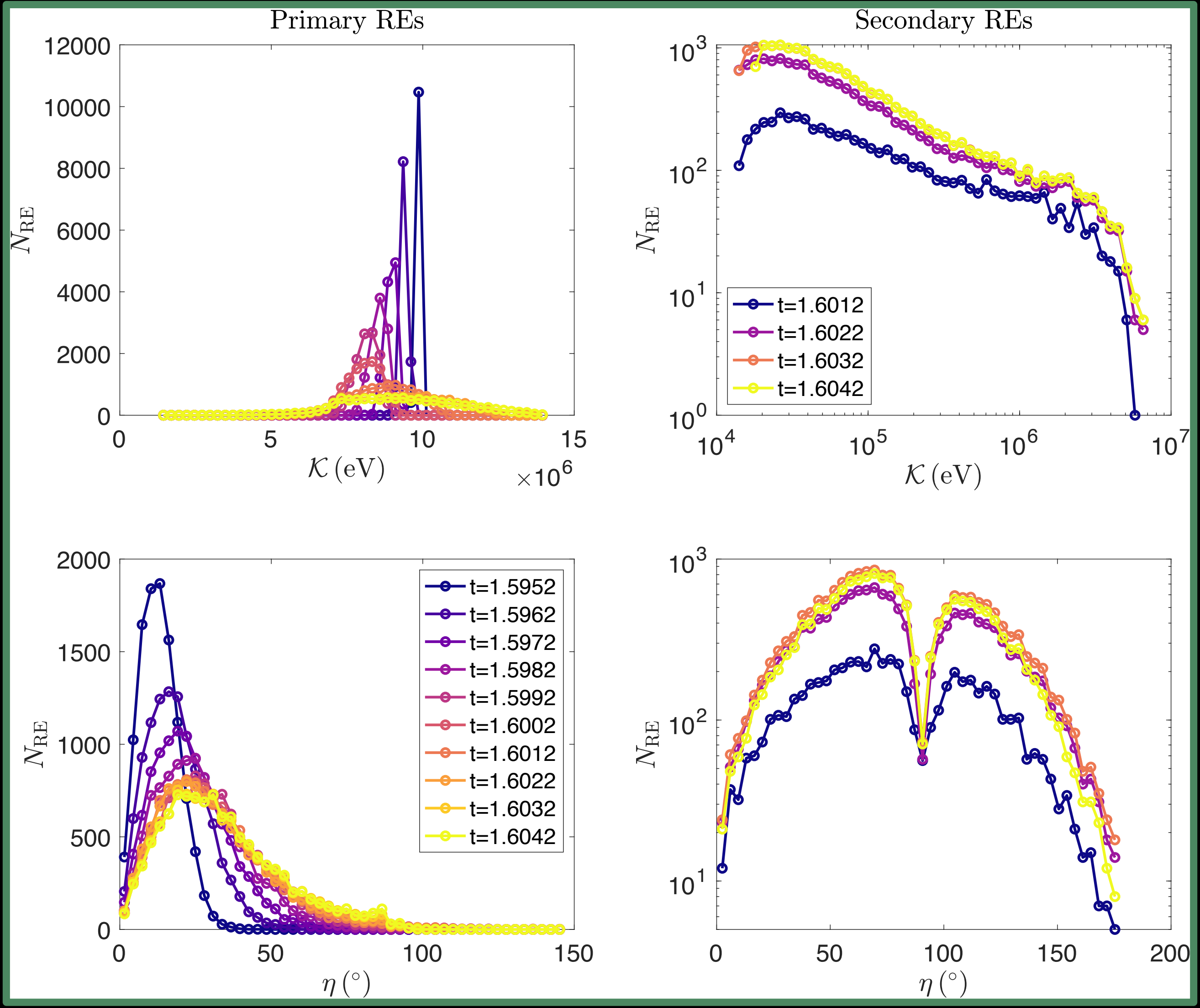

OAK RIDGE National Laboratory

Angle of incidence calculated from GC angle of incidence, pitch, and randomly-chosen gyrophase

- $\sin \Theta_i = -\cos \theta_{GC,i} \sin \eta_i \sin \chi_i + \sin \theta_{GC,i} \cos \eta_i > 0$

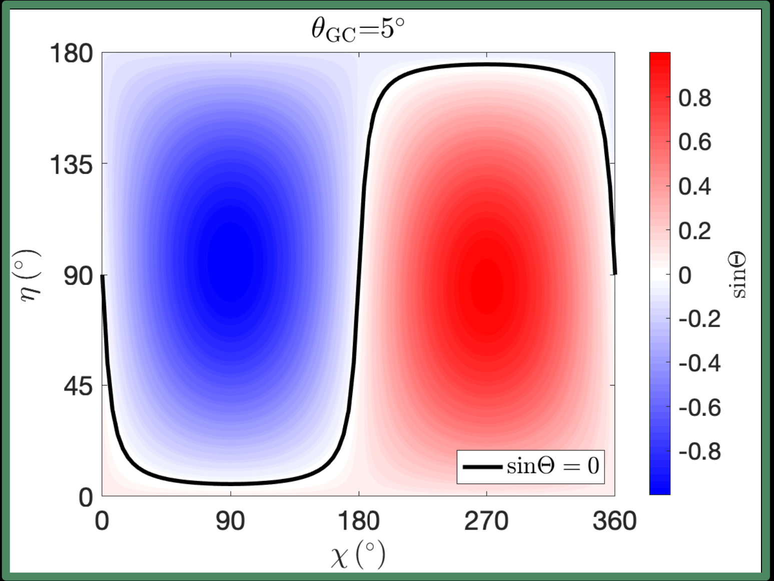

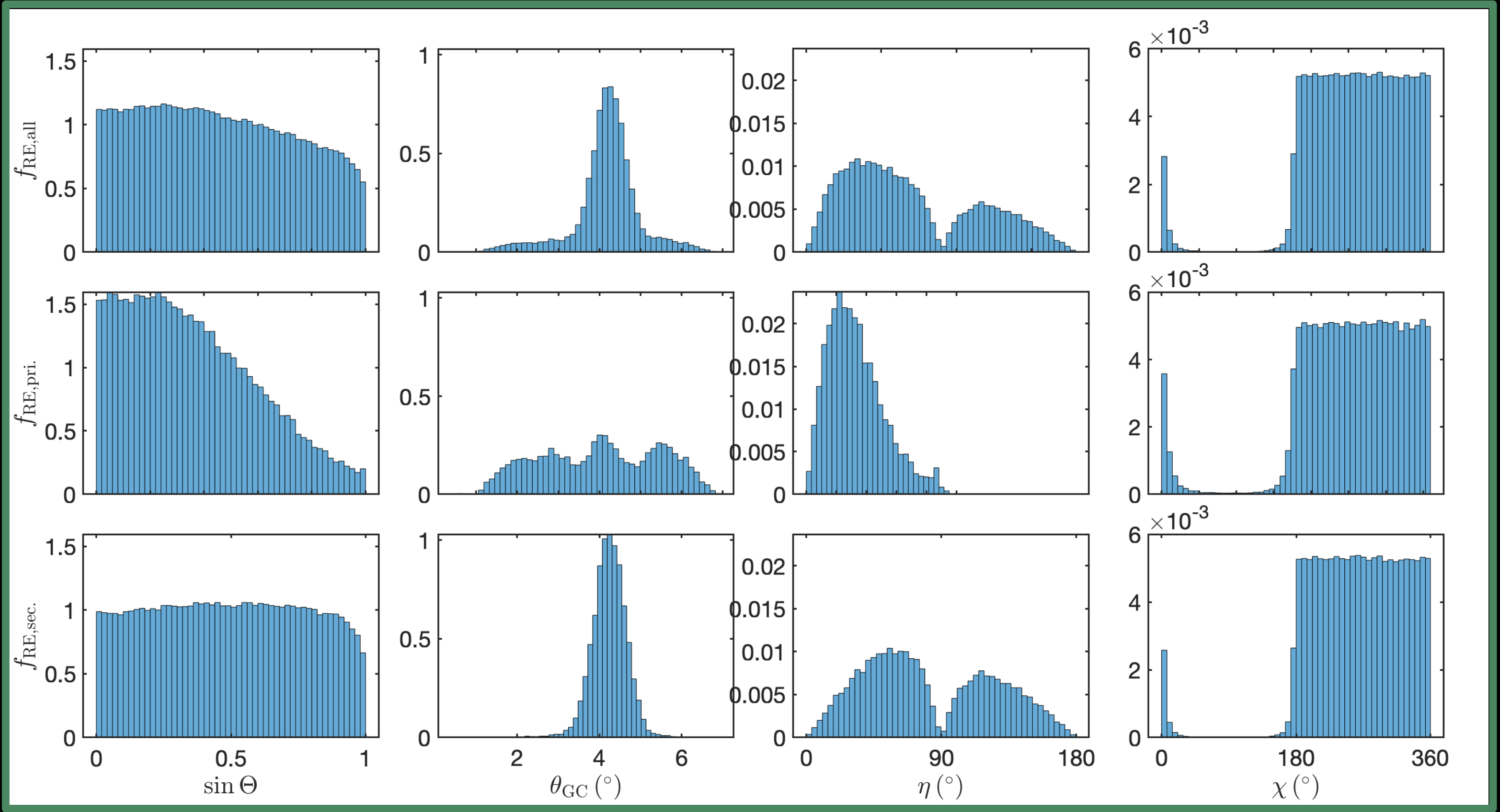

OAK RIDGE National Laboratory